

# A new terminal guidance sensor system for asteroid intercept or rendezvous missions



Joshua Lyzhoft<sup>a,\*</sup>, John Basart<sup>b</sup>, Bong Wie<sup>a</sup>

<sup>a</sup> Asteroid Deflection Research Center, Department of Aerospace Engineering, Iowa State University, Ames, IA 50011-2271, USA

<sup>b</sup> Department of Electrical and Computer Engineering, 351 Durham Center, Iowa State University, Ames, IA 50011-2271, USA

## ARTICLE INFO

### Article history:

Received 14 July 2015

Received in revised form

14 October 2015

Accepted 16 November 2015

Available online 27 November 2015

### Keywords:

Asteroid intercept terminal guidance

Visual and IR imaging sensor modeling and simulation

## ABSTRACT

This paper presents the initial conceptual study results of a new terminal guidance sensor system for asteroid intercept or rendezvous missions, which explores the use of visual, infrared, and radar devices. As was demonstrated by NASA's Deep Impact mission, visual cameras can be effectively utilized for hypervelocity intercept terminal guidance for a 5 kilometer target. Other systems such as Raytheon's EKV (Exoatmospheric Kill Vehicle) employ a different scheme that utilizes infrared target information to intercept ballistic missiles. Another example that uses infrared information is the NEOWISE telescope, which is used for asteroid detection and tracking. This paper describes the signal-to-noise ratio estimation problem for infrared sensors, minimum and maximum range of detection, and computational validation using GPU accelerated simulations. Small targets (50–100 m in diameter) are considered, and scaled polyhedron models of known objects, such as the Rosetta mission's Comet 67P/Churyumov–Gerasimenko, 101,955 Bennu, target of the OSIRIS-REx mission, and asteroid 433 Eros, are utilized. A parallelized ray tracing algorithm to simulate realistic surface-to-surface shadowing of a given celestial body is developed. By using the simulated models and parameters given from the formulation of the different sensors, impact mission scenarios are used to verify the feasibility for intercepting a small target.

© 2015 IAA. Published by Elsevier Ltd. All rights reserved.

## 1. Introduction

The Asteroid Deflection Research Center (ADRC) at Iowa State University has been developing a Hypervelocity Asteroid Intercept Vehicle (HAIV) concept to mitigate the impact threat of hazardous asteroids with short warning time [1–3]. An illustration of the proposed HAIV terminal intercept scenario is provided in Fig. 1. To demonstrate the feasibility of such a mission, a scaled polyhedron model of 433 Eros was used in [4] for a closed-loop optical navigation and guidance simulation study of the HAIV concept.

Similar concepts for hypervelocity asteroid intercepts using visual imaging autonomous guidance have been considered, such as the Don Quijote, Asteroid Impact and Deflection Assessment (AIDA), and the Impactor for Surface and Interior Science (ISIS) [5–8]. When visual tracking of a target is not available, an IR telescope/sensor might be required for a precision impact and mission success. It can be seen in Fig. 2 that size, with slight contribution from albedo, will affect the asteroid's signature in the IR regime, whereas for visual electromagnetic wave lengths asteroid size and albedo play a key role in object detection and observation.

An IR sensor array has been employed for the Exoatmospheric Kill Vehicle (EKV). This vehicle is designed to intercept ballistic missiles at hypervelocity speeds [9]. The on-board focal plane array used for EKV targeting consists

\* Corresponding author.

E-mail addresses: [jlyzhof@iastate.edu](mailto:jlyzhof@iastate.edu) (J. Lyzhof), [jpbasart@iastate.edu](mailto:jpbasart@iastate.edu) (J. Basart), [bongwie@iastate.edu](mailto:bongwie@iastate.edu) (B. Wie).

of a 256 by 256 structure with pixel pitch of 30  $\mu\text{m}$ , which is sensitive to long wave lengths (7–12  $\mu\text{m}$ ) and very long wave lengths (12–30  $\mu\text{m}$ ) IR emission [10]. During the EKV targeting process, the spacecraft receives information from the long wave IR sensor of the Space Based Infrared System (SBIRS) in low Earth orbit. By using the SBIRS, the detection range of the system is said to be about  $10^7$  km for an object emitting  $6 \times 10^8$  W/Ster. However, signal-to-noise ratios (SNR) vary depending on the probability of detection [11]. The EKV houses a 30 cm diameter optical system, which, with the IR detector, has an approximate detection range of 2000 km [12].

It has been shown in [13] which physical models are needed to estimate the SNR for a given detector and asteroid scenario in the N-band of IR wavelength. This formulation used an alternative definition for the SNR. A reference IR telescope, the Wide-field Infrared Survey Explorer (WISE), uses a Cassegrain like primary mirror to collect signal from objects of interest. A WISE telescope illustration can be seen in Fig. 3 [14].

## 2. Optics and sensors

Three types of sensors, along with their optical configurations, are studied for possible implementation to the HAIV. The instruments of interest herein are a visual sensor, an IR sensor, and a radar device. Typical parameters of these sensors are determined by estimating the SNR, which corresponds to a minimum or maximum detection distance, and characteristics of the optics to be implemented.

### 2.1. Classical Cassegrain telescope

A Classical Cassegrain telescope design is considered due to its simplicity and similarity to the NEOWISE infrared telescope design. An illustration of the Cassegrain telescope is given in Fig. 4, which will be the basis of the instrument's parameters. Given an effective focal length, a primary mirror focal length and diameter, and a back focus distance, telescope parameters are determined. It can be seen that baffling and glare stops are not considered.

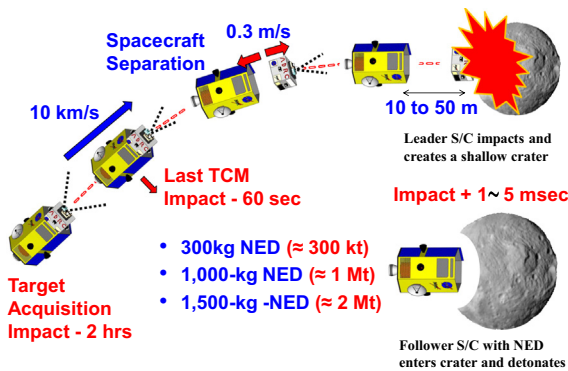


Fig. 1. A baseline terminal intercept scenario of a two-body HAIV carrying a nuclear explosive device (NED).

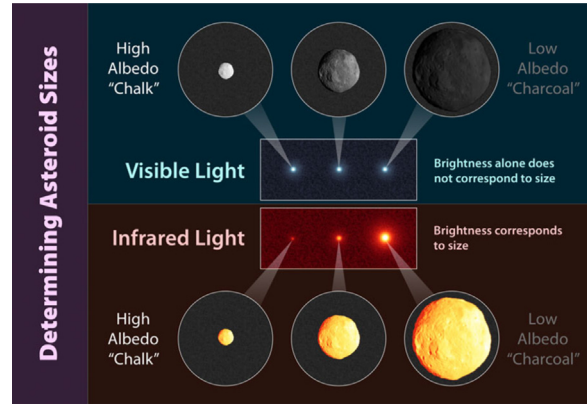


Fig. 2. Comparisons of optical and infrared images of asteroids with different sizes and albedos. Image courtesy of ([http://wise.ssl.berkeley.edu/gallery\\_asteroid\\_sizes.html](http://wise.ssl.berkeley.edu/gallery_asteroid_sizes.html)).

The magnification of the system is

$$M = \frac{F}{f_1} \quad (1)$$

where  $F$  and  $f_1$  are the system focal length and the primary mirror focal length. Once magnification is calculated, other parameters of this system are found. Given the back focus (distance from the primary mirror to the focal plane),  $b^*$ , the primary mirror focus intercept point is found as

$$p = \frac{F + b^*}{M + 1} \quad (2)$$

The overall distance from the secondary mirror to the focal plane, also known as the secondary to Cassegrain focus  $p'$ , is given by

$$p' = pM \quad (3)$$

From the Cassegrain focus, the mirror separation,  $B$ , is found as

$$B = p' - b^* \quad (4)$$

Another very important part of the Cassegrain telescope is to design the size of the secondary mirror. This diameter,  $D_s$ , can be found as

$$D_s = \frac{pD_o}{f_1} + \frac{BD_p}{f_1M} \quad (5)$$

where  $D_p$  is the minimum diameter of the image plane (not including thickness) and  $D_o$  is the primary mirror diameter. This correlates to the size of the imaging device, which is equivalent to the minimum dimension of the array. Eqs. (2) and (5) are given in Beish [15].

The radius of curvature (ROC) is found for both, the primary mirror and secondary mirror and is given by

$$R_1 = 2f_1 \quad (6)$$

and

$$R_2 = \frac{2}{\frac{1}{p} - \frac{1}{p'}} \quad (7)$$

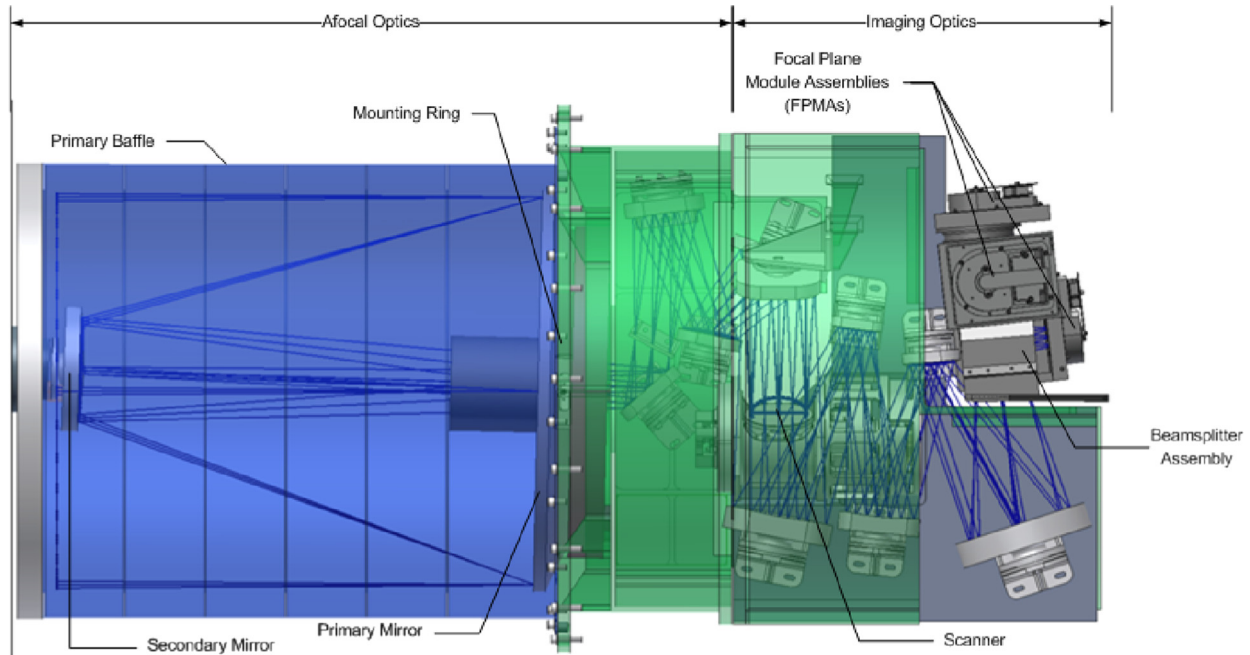


Fig. 3. Illustration of WISE telescope. Image courtesy of NASA/JPL.

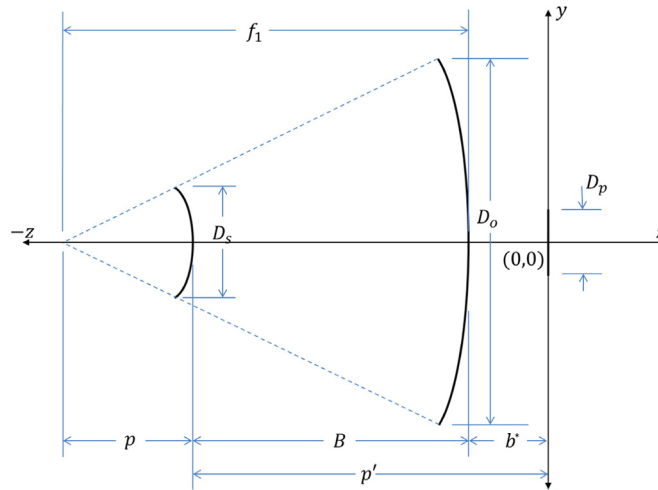


Fig. 4. Classical Cassegrain telescope design.

where  $R_1$  is the ROC for the primary mirror and  $R_2$  is the ROC for the secondary mirror [16,17]. By using the ROC of each mirror, the prescription for the two mirrors can be found by the formulas

$$z_1 = \frac{y_1^2}{2R_1} - b^* \quad (8)$$

$$z_2 = \frac{y_2^2/R_2}{1 + \sqrt{1 - (1 + b_2)(y_2/R_2)^2}} - (b^* + B) \quad (9)$$

and

$$b_2 = \frac{-4M}{(M-1)^2} - 1 \quad (10)$$

where  $z_1$  and  $z_2$  are face locations of the mirrors when the image plane array is located at the origin of a measurement,  $(-D_o/2) \leq y_1 \leq (D_o/2)$ , and  $(-D_s/2) \leq y_2 \leq (D_s/2)$  [17]. This is only valid in the case of a Classical Cassegrain telescope.

## 2.2. Visual sensor

A visual sensor is characterized herein. The first step of estimating the SNR is to integrate Planck's law for black body radiation over the visual band of electromagnetic spectrum, which gives the radiance. Fig. 5 illustrates the black body curves for the IR regime of interest for the electromagnetic spectrum. An assumption is made where IR and visual waves are not transmitted through the body

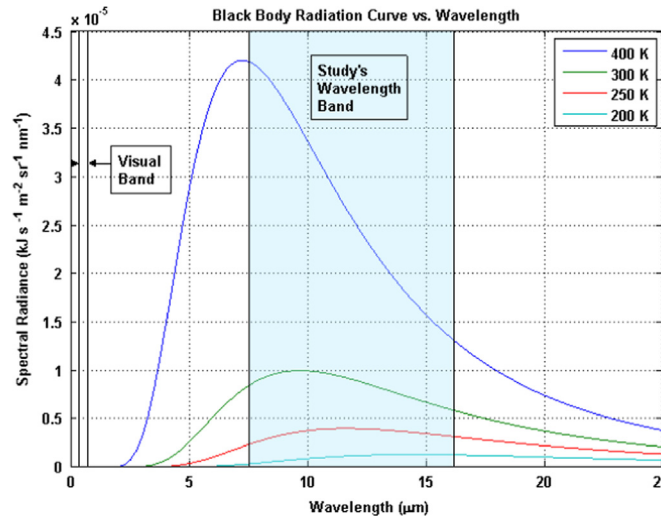


Fig. 5. Black body radiation for different temperature values in the IR regime.

and only reflected energy and emitted energy are considered. Below is the formulation of radiance ( $\text{W m}^{-2} \text{sr}^{-1}$ ) and irradiance ( $\text{W m}^{-2}$ ) for reflected energy. Radiance is given by

$$L_{Vs_i} = \int_{\lambda_1}^{\lambda_2} \frac{2hc^2}{\lambda^5} \frac{1}{e^{hc/k_B T_{\text{sun}} \lambda} - 1} d\lambda \quad (11)$$

where the temperature of interest is that of the sun,  $h$  is the Planck's constant ( $6.62606957 \times 10^{-34} \text{ m}^2 \text{ kg s}^{-1}$ ),  $c$  is the speed of light,  $k_B$  is the Boltzmann constant ( $1.3806488 \times 10^{-23} \text{ m}^2 \text{ kg s}^{-2} \text{ K}^{-1}$ ),  $\lambda_1$  is the lower bound wavelength, and  $\lambda_2$  is the upper bound wavelength. Since this is calculated, one must evaluate the radiance of the sun at the body, which is the irradiance multiplied by the sun's solid angle. A solid angle of an object is the area of its projection onto a sphere with some arbitrary radius corresponding to the distance between objects and is measured in steradians [18]. In this case, the radius is the distance from the sun to the object. However, the radius can also be from the object to the spacecraft, as will be used in the infrared situation. An assumption is made that the sun's solid angle can use a circular approximation, since the asteroid's distance from the sun is much larger than the radius of the sun. This leads to the incident irradiance at the object as

$$E_{Vs_i} = L_{Vs_i} \frac{\pi r_s^2}{d_{s/obj}^2} \quad (12)$$

where  $r_s$  is the radius of the sun and  $d_{s/obj}$  is the distance from the sun to the object. The irradiance of the reflected electromagnetic waves, from the object as seen by the spacecraft, is given by

$$E_{V_{\text{reflected}}} = \alpha_V \beta E_{Vs_i} \frac{\pi r_{obj}^2}{d_{obj/sc}^2} \quad (13)$$

where  $\alpha_V$  is the asteroid's visual albedo,  $r_{obj}$  is the radius of the object, and  $d_{obj/sc}$  is the distance from the object to the spacecraft. Here it is also assumed that the solid angle of the object can be given by a circular approximation due to

its radius being much smaller than the distance from the asteroid to the spacecraft. The variable,  $\beta$ , corresponds to the number of illuminated polyhedron faces seen by the spacecraft compared to the total number of faces illuminated by the sun. This variable will be discussed more in-depth later. The reflected energy's irradiance is estimated, and the emitted energy from the object is calculated.

The emitted energy from the body is very similar to reflected energy obtained by an integration of Planck's law using the asteroid temperature. A typical asteroid temperature, for objects approximately 1 AU away from the sun, is 300 K [19]. This will be used later for detection distances and simulations. The equation for emitted radiance is given by

$$L_{V_{\text{emitted}}} = \epsilon_V \int_{\lambda_1}^{\lambda_2} \frac{2hc^2}{\lambda^5} \frac{1}{e^{hc/k_B T_{obj} \lambda} - 1} d\lambda \quad (14)$$

where  $\epsilon_V$  is the object's visual emissivity. This assumes that there is no transitivity, which is the case for the infrared band as well. Once again, the irradiance can be found by multiplying the radiance by the solid angle (circular approximation), as follows:

$$E_{V_{\text{emitted}}} = L_{V_{\text{emitted}}} \frac{\pi r_{obj}^2}{d_{obj/sc}^2} \quad (15)$$

The total irradiance seen by the spacecraft is then given by

$$E_V = E_{V_{\text{reflected}}} + E_{V_{\text{emitted}}} \quad (16)$$

In general, the irradiance at the spacecraft from the visual emission can be neglected, therefore  $E_{V_{\text{emitted}}} \approx 0$ . From the irradiance, the photon flux, given in number of photons per square meter per second, is calculated as follows:

$$\Phi_V = \frac{E_V \lambda_{\text{max}}}{hc} \quad (17)$$

where  $\lambda_{\text{max}}$  is the wavelength of peak emission, which is a function of Wien's displacement constant and the Sun's temperature. By collecting the device parameters and the photon flux at the device, the signal given on the pixel

array in number of electrons is obtained as

$$S_{V_{signal}} = \Phi_V \tau_{opt} \eta G_V \tau_{int} N \pi \left( \frac{D_o}{2} \right)^2 \quad (18)$$

where  $a_{opt}$  is a coefficient from the optics,  $\tau_{opt}$  is the optics' efficiency,  $\eta$  is the device's quantum efficiency,  $G_V$  is the device's photoconductive gain,  $\tau_{int}$  is the device's integration time,  $N$  is the number of image samples, and  $D_o$  is the diameter of the primary mirror or lens. A similar expression can be found in [20]. Equation (18) is also used in IR signal formulation, which has IR specific variables. For the SNR to be calculated, the estimated standard deviations of the noise are found. The shot noise characteristics of the device are dictated by the following

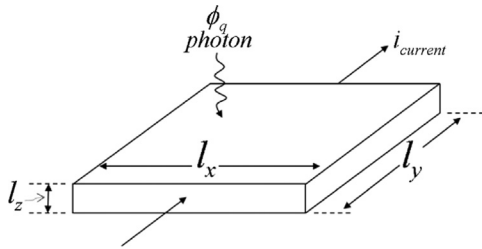


Fig. 6. A simple diagram of sensor pixel characteristics.

expression:

$$\sigma_{V_{shot}} = \sqrt{S_{V_{signal}}} \quad (19)$$

where the standard deviation is in number of electrons and follows Poisson statistics. Another noise contribution is caused by dark current. This noise also follows Poisson statistics and also is dictated by Arrhenius equations in the form of  $D = \kappa_1 e^{(\kappa_2/T)}$ , where  $T$  is the sensor temperature,  $\kappa_2$  represents a function of the activation energy of the material, and  $\kappa_1$  is the dark count per pixel per second. Using pixel 3 information found in [21], the parameters  $\kappa_1$  and  $\kappa_2$  can be calculated, which will be discussed later. These variables however, are sensor and pixel specific. The dark current standard deviation can then be written as

$$\sigma_{V_{dark}} = \sqrt{\frac{\kappa_1 n_{pix} \tau_{int} N e^{(\kappa_2/T_d)}}{D_V}} \quad (20)$$

where  $D_V$  is the dark count to electron conversion gain found in [22],  $T_d$  is the detector temperature, and  $n_{pix}$  is the total number of pixels. Similar forms of Eqs. (19) and (20) are found in [27]. These equations will also be applied to the IR sensor. Since these noise values are assumed to be statistically independent, the total noise standard deviation is described as

$$\sigma_{V_{noise}} = \sqrt{\sigma_{V_{shot}}^2 + \sigma_{V_{dark}}^2 + R_r^2} \quad (21)$$

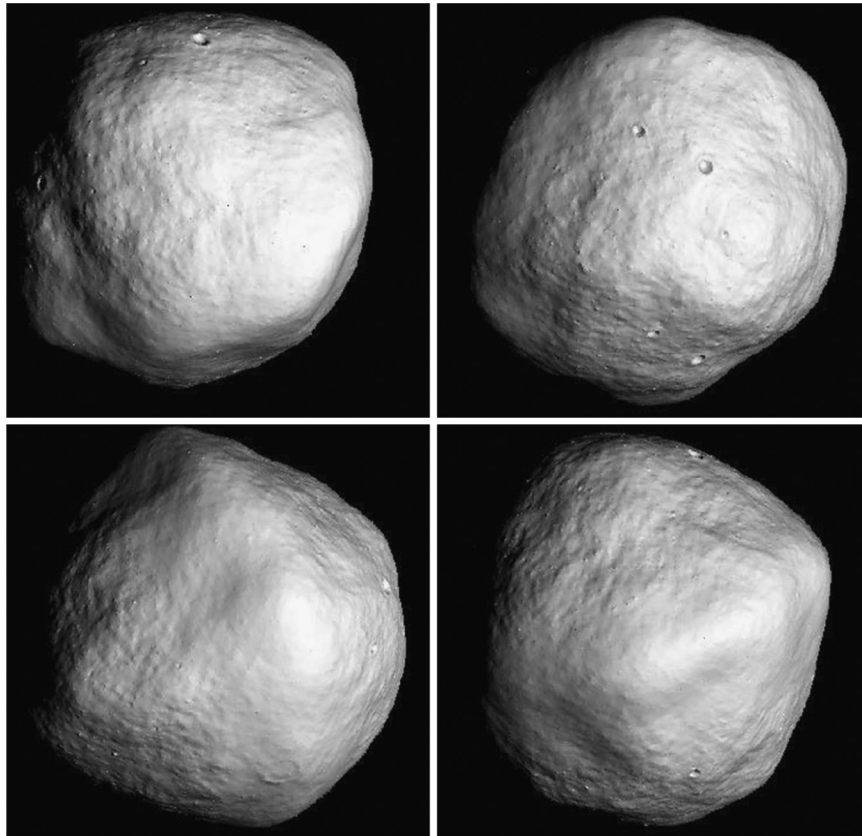


Fig. 7. Computer generated Bennu polyhedron model with shadowing.



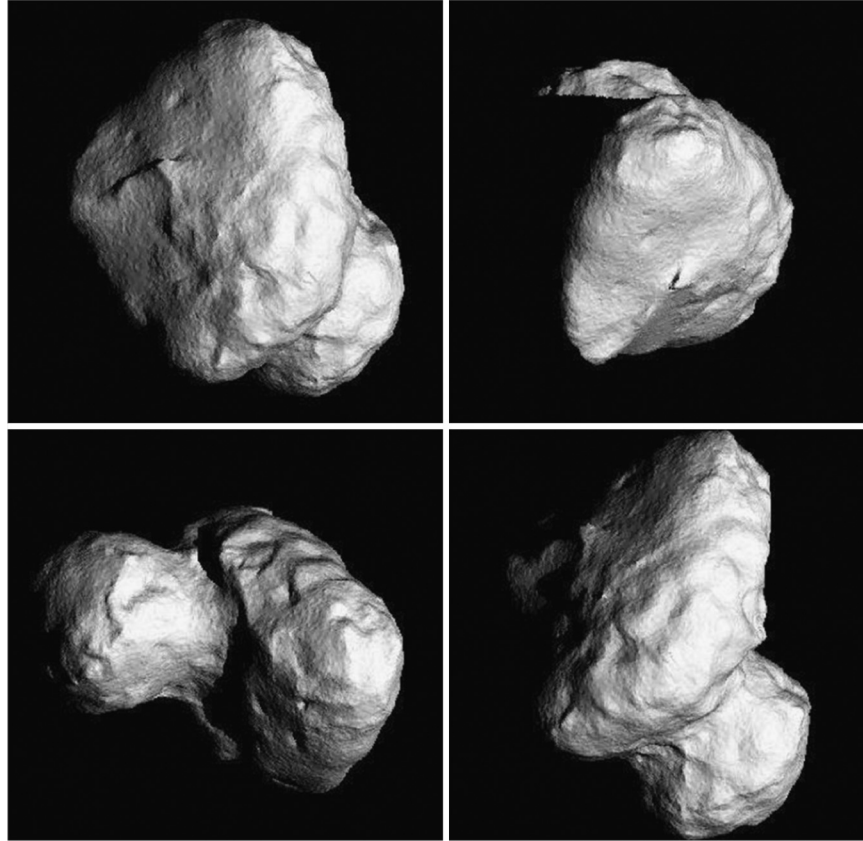


Fig. 8. Computer generated 67P/Churyumov-Gerasimenko polyhedron model with shadowing.

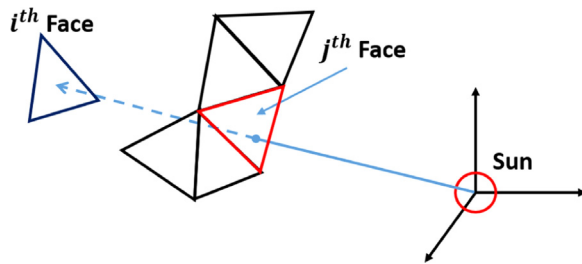


Fig. 9. Depiction of  $j$ th face intersecting the vector to the  $i$ th face.

where  $R_r$  is the read-in noise. This value is usually given as an RMS value measured in number of electrons. The final expression for the SNR in the visual band becomes

$$SNR_V = \frac{S_{V_{signal}}}{\sigma_{V_{noise}}} \quad (22)$$

### 2.3. Infrared sensor

Similar to the visual sensor, the IR device is simulated by also using Planck's law of black body radiation, which is integrated over the infrared wavelengths. However, the emissivity is taken into account. In Fig. 5, black body radiation curves for different asteroid temperatures are shown, and the band in a transparent blue represents the

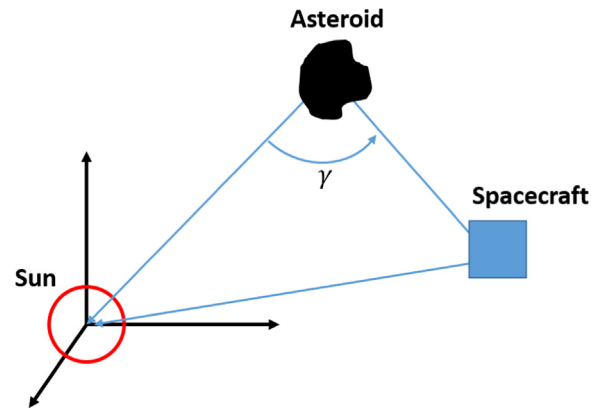


Fig. 10. Depiction of  $\gamma$  angle, where the axis is of the sun-fixed frame.

infrared wavelengths of this study. The radiance and irradiance for emitted and reflected radiation are given as

$$L_{IR_{emitted}} = \epsilon_{IR} \int_{\lambda_1}^{\lambda_2} \frac{2hc^2}{\lambda^5} \frac{1}{e^{hc/k_B T_{obj}\lambda} - 1} d\lambda \quad (23)$$

$$E_{IR_{emitted}} = L_{IR_{emitted}} \frac{\pi r_{obj}^2}{d_{obj/sc}^2} \quad (24)$$

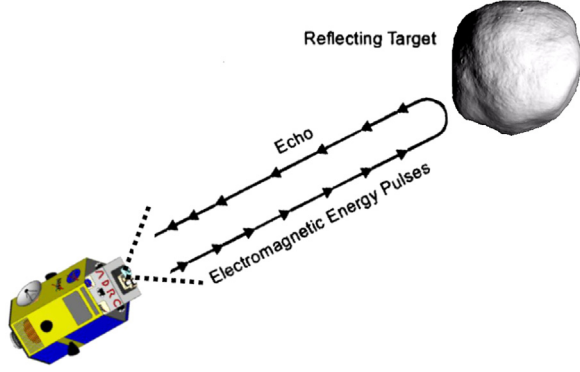


Fig. 11. Illustration of a monostatic radar system (not to scale).

$$L_{IRs_i} = \int_{\lambda_1}^{\lambda_2} \frac{2hc^2}{\lambda^5} \frac{1}{e^{hc/k_B T_{sun}\lambda} - 1} d\lambda \quad (25)$$

$$E_{IR_{reflected}} = \alpha_{IR} \beta L_{IRs_i} \frac{\pi r_s^2}{d_{s/obj}^2} \frac{\pi r_{obj}^2}{d_{obj/sc}^2} \quad (26)$$

$$E_{IR} = E_{IR_{emitted}} + E_{IR_{reflected}} \quad (27)$$

where  $\epsilon_{IR}$  is the IR emissivity of the object,  $\alpha_{IR}$  is the object's IR albedo,  $\lambda_1$  and  $\lambda_2$  are the IR lower and upper bound wavelengths. Note that these equations must be integrated over the infrared spectrum regime of interest. To find the radiance for reflected energy and emitted energy, they are not integrated over the visual spectrum like in the visual camera section, but over infrared wavelengths. Following similar steps from that of the visual camera, the photon flux and signal are described as follows:

$$\Phi_{IR} = \frac{E_{IR} \lambda_{max}}{hc} \quad (28)$$

$$S_{IR_{signal}} = \Phi_{IR} \tau_{opt} \eta G_{IR} \tau_{int} N \pi \left( \frac{D_{mirror}}{2} \right)^2 \quad (29)$$

where the  $\lambda_{max}$  is the wavelength of peak emission, which is a function of Wien's displacement constant and object's temperature and  $G_{IR}$  is the IR device gain. With signal photons known, noise characteristics need to be developed.

Four types of noise sources are considered herein: shot noise, dark current noise, Johnson noise, and generation-recombination noise. The standard deviations of each noise can be described as

$$\sigma_{IR_{shot}} = \sqrt{S_{IR_{signal}}} \quad (30)$$

Similarly, the dark current noise for the infrared sensor can be expressed in the Arrhenius form. The parameters  $\kappa_1$  and  $\kappa_2$  are found by using material specific information. For later comparison to the WISE telescope, a silicon arsenide (Si:Ar) detector is used. Information regarding the dark current electron count per pixel can be found in [23]. However, the Si:Ar detector parameters are that of the James Web Space Telescope's (JWST) Mid-Infrared Instrument (MIRI). This will be discussed in a later

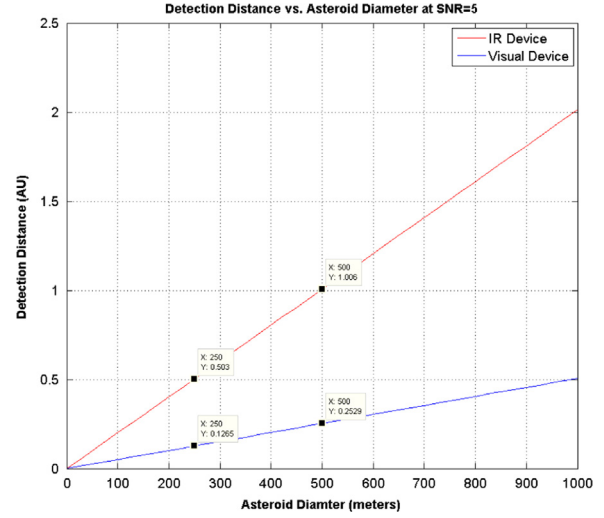


Fig. 12. Detection distances vs. asteroid diameter of IR and visual band sensors using WISE telescope parameters.

section. The dark current noise is then expressed as

$$\sigma_{IR_{dark}} = \sqrt{\frac{\kappa_1 n_{pix} \tau_{int} N e^{(\kappa_2/T_d)}}{D_V}} \quad (31)$$

where again,  $D_V$  is the dark count per electron gain for the detector. To reiterate, the parameters  $\kappa_1$  and  $\kappa_2$  in the IR detector are not the same as in the visual detector section:

$$\sigma_{IR_{johnson}} = \sqrt{\frac{2k_B n_{pix} T_d \rho l_y N G^2}{l_x l_z R_{sp}^2 \tau_{int}}} \quad (32)$$

where  $(l_x, l_y, l_z)$  are pixel dimensions,  $R_{sp}$  is voltage to electron conversion, and  $\rho$  is the resistivity. Typical values for  $R_{sp}$  can be found in [24]. The resistivity is the inverse of conductivity and is sensitive to detector temperature. Material information of the Si:Ar detector at low temperatures is taken from [25]. In general, for semiconductors, the resistivity follows an Arrhenius form [26]. An expression for  $\rho$  is

$$\rho = \rho_o e^{E_a/k_{Be} T_d} \quad (33)$$

where  $\rho_o$  is the resistivity as detector temperature goes to infinity,  $E_a$  is the material activation energy given in electron volts, and  $k_{Be}$  is Boltzmann's constant in electron volts per kelvin.

$$\sigma_{IR_{GR}} = G \sqrt{2\eta \Phi_{IR} \tau_{opt} A_d N \tau_{int}} \quad (34)$$

where  $A_d$  is the area of the detector. Similar forms of Eqs. (30) through (34) can be found in [27,28]. An illustration of a simple sensor pixel can be seen in Fig. 6. If the noises are assumed to be statistically independent of each other, then the total noise standard deviation for the infrared regime is given by

$$\sigma_{IR} = \sqrt{\sigma_{IR_{shot}}^2 + \sigma_{IR_{dark}}^2 + \sigma_{IR_{johnson}}^2 + \sigma_{IR_{GR}}^2} \quad (35)$$

From the formulated IR signal and noise equations, the SNR in the infrared band of interest takes the same form as that of the visual band, which is the ratio of estimated

**Table 1**

Visual sensor design results and asteroid parameters.

Instrument characteristics	Value	Asteroid parameters	Value
$F$	1.35 m	$T_{ast}$	300 K
$M$	8	$r_{ast}$	25 m
$D_o$	0.2 m	$d_{s/obj}$	1.496e8 km
$b^*$	0.0115 m	$d_{obj/sc}$	$\approx 7.75e5$ km
$\eta$	0.7	$\alpha$	0.25
$G_V$	6.83	$\beta$	1
$\tau_{optics}$	0.504		
$N$	1		
$\tau_{int}$	1 s		
$T_d$	230 K		
$R_r$	10 e/pixel/s		
$D_v$	2.8 DN/e		
$\kappa_1$	1.03212649e7 DN/pixel/s		
$\kappa_2$	−3752.58 K		
$n_{pix}$	1024 × 1024 = 1,048,576 pixels		
Pixel pitch	18 $\mu$ m		
$\lambda_1, \lambda_2$	380, 800 nm		

signal to the calculated noise standard deviation, given by

$$SNR_{IR} = \frac{S_{IR,signal}}{\sigma_{IR}} \quad (36)$$

#### 2.4. Image rendering and $\beta$ calculation

The visual camera is simulated by incorporating the albedo of a given target and assigning values to polyhedron shape model faces according to the direction of the sun vector with the asteroid. This sun vector,  $\hat{S}$ , is the unit vector pointing from the sun to the target [29]. Each polyhedron face coefficient is described as

$$C_i = \begin{cases} k_d (\hat{N}_i \cdot -\hat{S}) + k_a & \text{if } (\hat{N}_i \cdot -\hat{S}) > 0 \\ 0 & \text{if } (\hat{N}_i \cdot -\hat{S}) \leq 0 \end{cases} \quad (37)$$

where  $i$  is the face index,  $\hat{N}_i$  is the outward pointing unit normal vector of each face,  $k_d$  is the diffuse lighting coefficient associated with the object's albedo, and  $k_a$  is the ambient lighting coefficient. By using this vector, including a ray trace algorithm for shadowing, and exploiting the advantages of parallel computing, realistic images can be generated quickly. Such images can be seen in Figs. 7 and 8. These images, however, are computed in grayscale and are not usually seen in real imaging situations. Pixelation, blurring, and aberrations would be presented in a full realistic situation.

These computer generated images are depictions of Bennu and Comet 67P/Churyumov-Gerasimenko (Comet 67P/C-G), which are taken at different times within a simulation where the respective body is rotating about a general axis. As can be seen in these figures, there is crater shadowing. The shadowing is done by a GPU accelerated ray tracing algorithm. By applying this algorithm, the face coefficient for any given face  $i$  becomes zero under the following condition: there exists a face  $j$  that intersects the vector from the sun to the  $i$ th face, where the intersecting  $j$ th face is located between the sun and the  $i$ th face. An illustration of the face intersection can be seen in Fig. 9.

This shadowing effect will help simulating landing on a target or tracking rendezvous locations.

The  $\beta$  coefficient, which correlates to the estimated solid angle for a non-flat surfaced convex shape (cuboid), is estimated as

$$\beta = \frac{\text{Total number of illuminated faces seen by camera}}{\text{Total number of illuminated faces}} \quad (38)$$

This assumption of a non-cuboid shape must be made for the above to hold. Instances could arise where all of the illuminated faces of the object could be seen even though there is an incident angle. If this were to occur, Eq. (38) shows that the radiation from the body would be the same as if the incident angle were zero. An over approximation of the detection distance or SNR at a certain range would be caused by these flat-surfaced shapes.

However, if one is not using a polyhedron model, an approximation of the  $\beta$  coefficient can be made. This parameter uses the angle between the vector from the asteroid to the sun and the vector from the asteroid to the spacecraft, which will be denoted as  $\gamma$ , measured in radians. Moreover, this approximation is used primarily for spherical shapes. When different geometries are present, such as Comet 67P/C-G, other approximations should be used. A depiction of this angle can be seen in Fig. 10. The  $\beta$  coefficient approximation is

$$\beta \approx \cos\left(\frac{\gamma}{2}\right) \quad (39)$$

#### 2.5. Radar

Object range determination for a monostatic system (transmitter and receiver are collocated) is found. An illustration of a monostatic system is depicted in Fig. 11. The radar expression is manipulated to find the maximum detection distance. A minimum detection distance is also required since there is a transition from the near-field to the far-field of the signal. The transition distance from the near-field to the far-field is given in [30]. There is still



**Table 2**

IR device design results and asteroid parameters.

Instrument characteristics	Value	Asteroid parameters	Value
$F$	1.35 m	$T_{ast}$	300 K
$M$	8	$r_{ast}$	25 m
$D_0$	0.2 m	$d_{s/obj}$	1.496e8 km
$b^*$	0.0115 m	$d_{obj/sc}$	$\approx 7.55e5$ km
$\eta$	0.7	$\epsilon$	0.9
$G_{IR}$	6.83	$\beta$	1
$\tau_{optics}$	0.504		
$N$	1		
$\tau_{int}$	1 s		
$T_d$	10 K		
$\kappa_1$	8.505735e13 e/pixel/s		
$\kappa_2$	–225.5617 K		
$E_a$	0.01943 eV		
$R_{sp}$	0.5e–6 V/e		
$\rho_0$	7.99742e–9 $\Omega$ m		
$n_{pix}$	1024 $\times$ 1024 = 1,048,576 pixels		
Pixel pitch	18 $\mu$ m		
$\lambda_1, \lambda_2$	7.5, 16.5 $\mu$ m		

**Table 3**

Asteroid detection results for a visual sensor.

Parameters	Value
Geometric optics pixel fill	< 1
Visual magnitude	$\approx 12.5$
$SNR_V$	$\approx 10.06$

signal received in the nearfield, but may give incorrect values. These two equations are given by

$$R_{max} = 4 \sqrt{\frac{P_t K_{losses} (G_R)^2 \lambda_R^2 \sigma_R (N_R)^{1/2}}{(4\pi)^3 k_B T_e \Delta f (SNR_R)}} \quad (40)$$

$$R_{min} = \frac{2D_R^2}{\lambda_R} \quad (41)$$

where  $P_t$  is the peak pulse power transmitted,  $K_{losses}$  are the losses of the device,  $G_R$  is the antenna gain,  $\lambda_R$  is the radar wavelength,  $\sigma_R$  is the object's radar cross section,  $N_R$  is the number of samples,  $T_e$  is the equivalent noise temperature,  $\Delta f$  is the bandwidth,  $(SNR_R)$  is the desired signal-to-noise ratio, and  $D_R$  is the primary signal-collecting dish's diameter (assuming a circular dish). Variables of other devices should not be confused with radar parameters.

### 3. Sensor comparison and simulation results

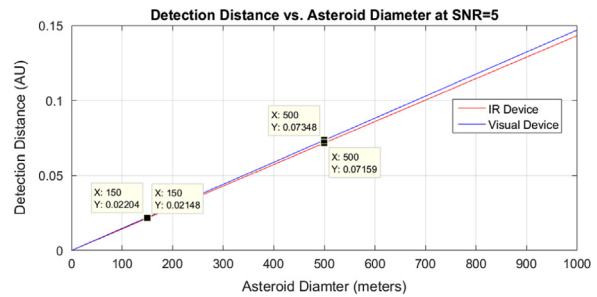
#### 3.1. Sensor comparison

Comparison of the sensing devices discussed in the preceding sections is provided herein. This entails the asteroid's detection distance, which corresponds to device's SNR, and image representation given in SNR values. These images are plotted using a Matlab program and the calculated standard deviation of the noise.

**Table 4**

Asteroid detection results for an IR sensor.

Parameters	Value
Geometric optics pixel fill	< 1
Visual magnitude (N band)	$\approx 4.47$
$SNR_{IR}$	$\approx 10.04$

**Fig. 13.** Detection distances vs. asteroid diameter of IR and visual band sensors.

#### 3.1.1. WISE telescope comparison

Parameters for the WISE telescope are used to compare with the literature and visual sensors. These parameters for the Si:Ar detector and optics can be found in [23,31,32]. By using a detector temperature of 8 K, integration time of 8.8 s, and other parameters of the Si:Ar detector and WISE optics, it was found that a 250 m diameter object could be detected with a SNR of 5 at approximately 0.5 AU. This confirms what is stated in [33]. However, a few assumptions are made for the asteroid: the asteroid is spherical, has an emissivity of 0.9, which is similar to values in [34,35], but is lower than the values given in [36,37], and has a  $\beta$  coefficient value of one. Fig. 12 shows the detection distance compared to a telescope with comparable optics. The visual sensor has a read noise of 10  $e^-$ /s/pixel RMS, detector temperature of approximately 230 K, integration

time of 8.8 s, and other parameters to that of the IR sensor and optics. It can be seen that the detection distance is linear with the asteroid diameter. This is due to the solid angle approximation using a circumscribing sphere.

### 3.1.2. Infrared and visual sensor comparison

Various parameter values of the visual and IR detection devices are kept very similar to those of the NEOWISE telescope, except for a reduction in primary mirror size and operating temperature. By using the formulation for the signal-to-noise ratio and the values given in Tables 1 and 2, the results for the SNR value of approximately 5 are provided in Tables 3 and 4. Results illustrate the geometric pixel fill corresponding to the largest dimension of the object, as well as the visual magnitude. These tables show that the geometric pixel fill of the object is less than one, which means there is no object detail resolved but detected. The visual magnitude is calculated from the flux density of the object in both IR and visual wavelengths. In both cases, the reference celestial object is Vega, with an assumed visual magnitude of 0.03 (N band and visual band).

Notice that the distance from the object to the spacecraft is almost identical between the visual and IR sensor.

**Table 5**  
A reference radar design.

Instrument characteristics	Value
$P_t$	500 W
$K_{losses}$	0.55
Scale	1/10
$G_R$	8.0568e5
$\lambda_R$ (Scaled)	3.5 mm
$\sigma_R$ (Scaled)	340 m <sup>2</sup>
$N_R$	1000
$t_s$ (Pulse width)	1 $\mu$ s
$T_e$	70 K
$\Delta f$ (1/ $t_s$ )	1.0e6 Hz
(SNR <sub>R</sub> )	10
$D_R$	1 m

This means that the IR device can detect a 50-m object, with N band emissivity of 0.9, at about the same distance as the visual device. The detection distances using an IR sensor are not as great as the visual sensor, which is primarily due to the increase of operation temperature. Moreover, in the visual band, the albedo of the asteroid is set at 0.25, which is a high value for an asteroid. If the phase angle were to be increased, correlating to a smaller  $\beta$  coefficient, the visual sensor would not outperform the IR sensor for these instrument characteristics. With these parameters, the detection distances and selected asteroid sizes can be seen in Fig. 13. In these plots, the lines for detection distance are linear due to the assumption of the solid angle being subtended by a circular approximation, along with other approximations using polyhedron face plane projections.

As stated previously, parameters of the radar device are different from the other two sensing devices. By using the equations describing the radar, an estimation of minimum and maximum detection distances can be found. A scaled Bennu model is used here to evaluate the radar performance. Bennu is scaled by 1/10, resulting in a diameter around 50 m. When scaling Bennu, the transmitted signal's wavelength must also be scaled by the same factor, if similar detection distances are desired. At a wavelength of 3.5 cm, a unscaled Bennu has a radar cross-section of

**Table 6**  
Comparison of IR and visual sensors during asteroid intercept phase (optical components are the same as in previous comparison).

Simulation results	IR	Visual
$d_{obj/sc}$ at 2 h	7.2e4 km	7.2e4 km
Visual magnitude at 2 h	−0.654	7.312
Geom. pixel fill at 2 h	< 1	< 1
SNR at 2 h	1.098e3	1.105e3
$d_{obj/sc}$ at 60 s	600 km	600 km
Visual magnitude at 60 s	−11.10	−3.134
Geom. pixel fill at 60 s	≈ 7	≈ 7
SNR at 60 s	1.09e6	4.145e5

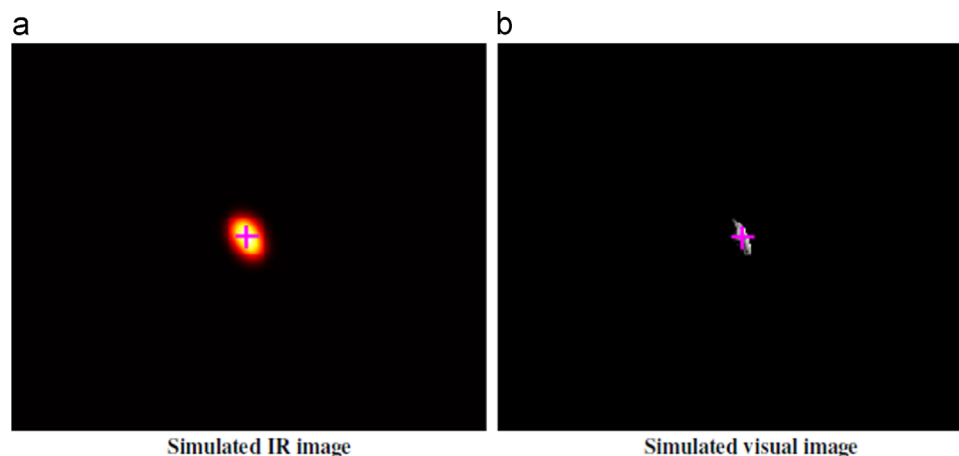


**Fig. 14.** Examples of IR and visual sensor images at 60 s prior to final impact.

$3.4 \times 10^4 \text{ m}^2$ , which correlates to a scaled  $\sigma_R$  of 340 m and a wavelength of 3.5 mm. This creates a needed wavelength that is near the edge of the radar regime of the electromagnetic spectrum but is still obtainable.

By using the values in Table 5, the radar equations result in a maximum detection distance of  $9.062 \times 10^2 \text{ km}$ . However, the minimum distance is dictated by the far-field and near-field transition, if there are no filtering techniques applied. This minimum distance before nearfield

transition measures 571 m. Rendezvousing with a target body and landing on its surface would need a radar device that has a lower minimum detection range.

### 3.2. Terminal guidance simulation results

Hypervelocity intercept missions are simulated using a scaled 433 Eros polyhedron model. The points of interest are at two hours and 60 s before impact. Fig. 14 compares the visual and infrared sensors at 60 s before asteroid intercept. These simulated images were obtained by using the parameters given in Tables 1 and 2, along with Cassegrain telescope design. It can be seen that the asteroid does not fill many pixels on the sensor array. The calculated amount of pixels filled for the maximum dimension of the asteroid can be seen in Table 6. This table also includes the SNR for both times of interest. Two hours before impact, each sensor array displays sub-pixel pixel fill. However, at 60 s before impact, the horizontal pixel fill is at approximately 37 pixels. In both the sensor scenarios, 2 h or 60 s before impact, the pixel fill does not provide detailed target images.

It can be seen that the SNRs at two hours before impact are quite different for both devices. At this point, the IR device can discern the asteroid, whereas the visual device does not have an adequate SNR. This shows for lower albedo asteroids, which are small and have higher emissivity, that the IR device may out-perform the visual

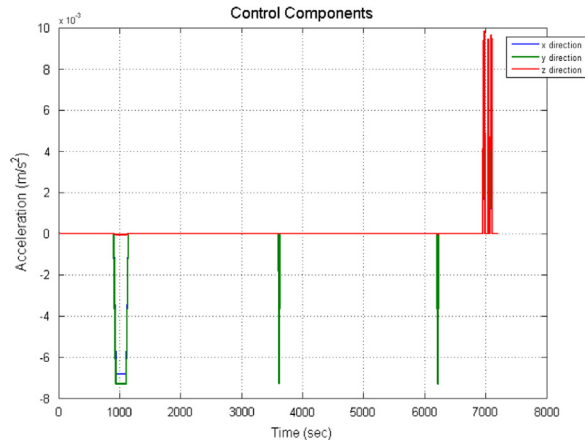


Fig. 15. Control acceleration time history of an IR-based terminal guidance system ( $t=0$  implies 2 h before impact).

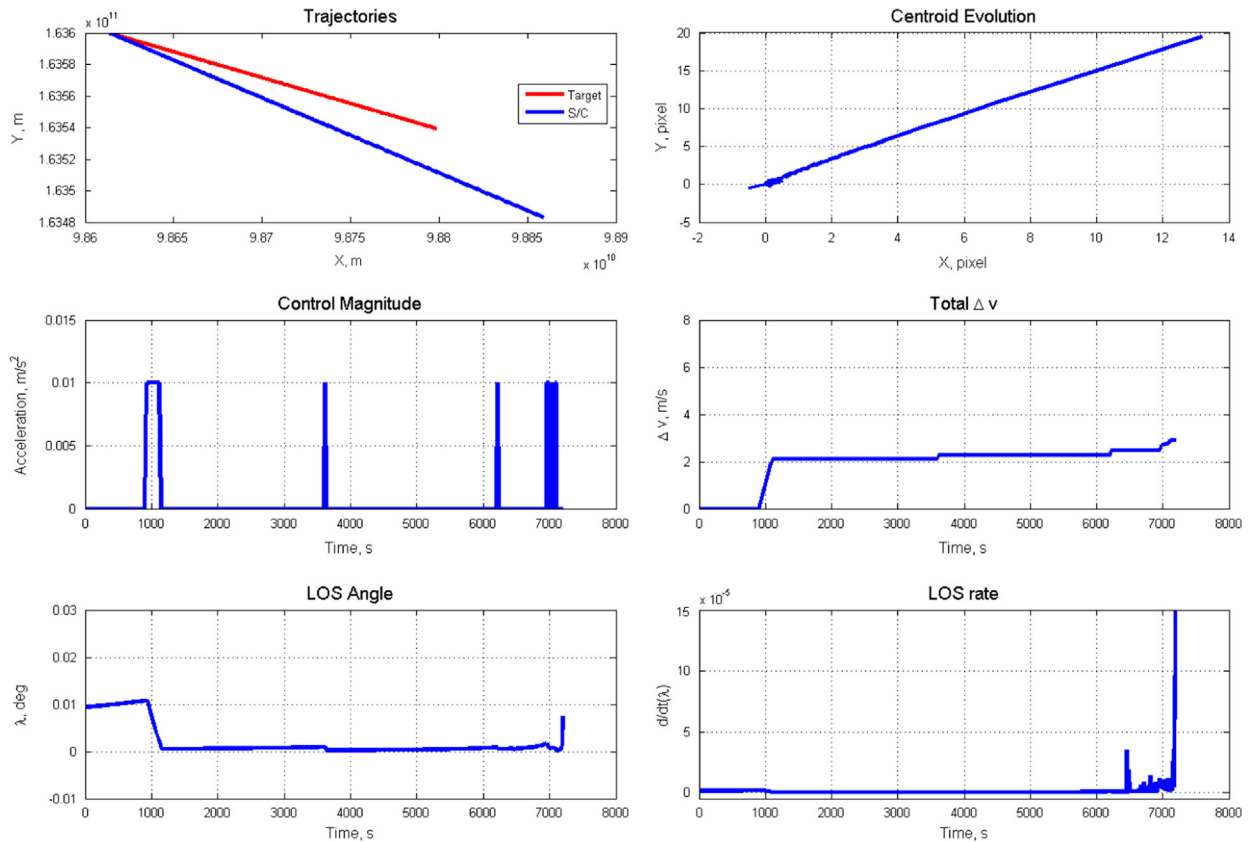
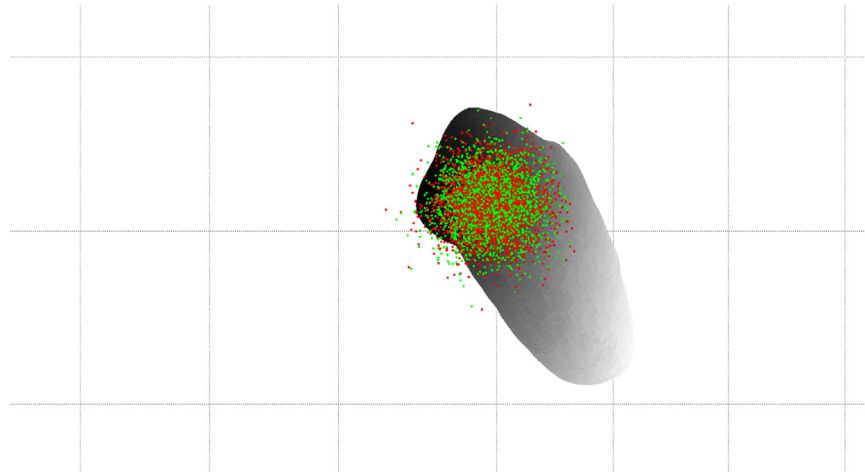


Fig. 16. Mission specific variables vs. time (or pixel centroid locations) for an IR-based terminal guidance system ( $t=0$  implies 2 h before impact).



**Fig. 17.** Monte Carlo simulation result for intercepting a 50-m asteroid using an IR-based terminal guidance system. (For interpretation of the references to color in this figure caption, the reader is referred to the web version of this paper.)

device. Consequently, the guidance algorithms use the information from the IR device and radar. Radar is used once the distance from the asteroid to the spacecraft is sufficient for radar detection, which was stated to be about 900 km.

For the guidance simulations, a hybrid algorithm is used. This includes kinematic intercept guidance, which uses predetermined control pulses and proportional navigation. During the beginning of the terminal phase of the mission, the spacecraft undergoes kinematic impulse guidance, and once a sufficient amount of pixels is filled on the sensor array by the target, the guidance algorithm is switched to proportional navigation guidance to ensure mission success. A depiction of the control accelerations can be seen in Fig. 15. Spacecraft  $\Delta v$  requirements and other mission specifications can be seen in Fig. 16. For this scenario, the velocity requirement is small, because this is done during the terminal phase of the mission. These requirements assume that the major trajectory maneuvers have been completed prior to the terminal phase. The resulting intercept speed is approximately 10 kilometers per second.

Using this same control acceleration, at 60 s before impact, the spacecraft will separate into a fore and aft body system [38]. At this separation time, a position and velocity error are placed on the fore and aft bodies. This simulation is conducted 3000 times. After these simulations, approximately 98.5 percent of the fore bodies and 98.7 percent of the aft bodies impact in the IR case. In comparison, only 93.4 percent impacted of both fore and aft bodies for the visual case. A depiction of these simulations are shown in Fig. 17. This figure, green dots represent the fore body, while red dots represent the aft body. In this scenario, the impact percentage utilizing an IR sensor barely outperformed the visual camera case. This is due to the sun-asteroid-spacecraft phase angle. If the  $\beta$  coefficient were to be closer to zero, larger phase angle, less light would be illuminating the surface of the asteroid in the spacecraft's line-of-sight, which would cause a lower percentage of successful impacts.

#### 4. Conclusion

In this paper, the signal-to-noise ratio estimation and detection distance estimation for IR and visual sensing devices have been examined for asteroid intercept/rendezvous applications. In addition, estimation of the solid angle of an object due to shadowing was studied, which relates to object irradiance. By following the procedures described in this paper, maximum detection distances were found for all three sensing devices. These distances, corresponding to a 50-m asteroid, were estimated to be  $7.75 \times 10^5$  km for the visual device,  $7.55 \times 10^5$  km for the IR device, and 906.2 km for the radar. These results show that for an asteroid with an IR emissivity of 0.9 and a visual albedo of 0.25, the IR sensing device detects the asteroid at a distance approximately the same as the visual sensing device. To evaluate the performance of a terminal guidance system equipped with such sensors, Monte Carlo simulations were performed, which resulted in approximately 98.5% impact success using an IR device and only 93.4% for a visual device. Further research must consider more accurate solid angle approximations, as well as device functionality in close asteroid proximity situations and asteroid polyhedron gravitation.

#### References

- [1] B. Wie, Hypervelocity nuclear interceptors for asteroid disruption, *Acta Astronaut.* 90 (2013) 146–155.
- [2] A. Pitz, B. Kaplinger, G. Vardaxis, T. Winkler, B. Wie, Conceptual design of a hypervelocity asteroid intercept vehicle (HAIV) and its flight validation mission, *Acta Astronaut.* 94 (2014) 42–56.
- [3] B. Barbee, B. Wie, M. Steiner, K. Getzandanner, Conceptual design of a flight demonstration mission for hypervelocity asteroid intercept vehicle (HAIV), *Acta Astronaut.* 106 (2015) 139–159.
- [4] J. Lyzhoft, M. Hawkins, B. Kaplinger, B. Wie, GPU-Based optical navigation and terminal guidance simulation of a hypervelocity asteroid impact vehicle (HAIV), AIAA-2013-4966, AIAA Guidance, Navigation, and Control Conference, Boston, MA, 19–22 August 2013.
- [5] Juan L. Cano, et al., Mission analysis for the Don Quijote phase-a study, in: Proceedings of the 58th Congress of the International Astronautical Federation, Hyderabad, India, 2007.

- [6] Andrés Gálvez, Ian Carnelli, ESA Studies on the Don Quijote NEO mission: dealing with impact uncertainties, in: Proceedings of the 56th International Astronautical Congress, Fukuoka, Japan, 2005.
- [7] A.F. Cheng, et al., AIDA: asteroid impact & deflection assessment, in: 64th International Astronautical Congress, IAC-13-A3.4.8, Beijing, China, 23–27 September 2013.
- [8] Steven R. Chesley, et al., The ISIS mission concept: an impactor for surface and interior science, in: International Academy of Astronautics Planetary Defense Conference, IAA-PDC2013-04-01, Flagstaff, Arizona, USA, 15–19 April 2013.
- [9] B. Wie, B. Barbee, et al., An Innovative Solution to NASA's Neo Impact Threat Mgrand Cand Flight Validation Mission Architecture Development, NASA Grant and Cooperative Agreement Number: NNX12AQ60G, 9 December 2014, ([http://www.nasa.gov/sites/default/files/files/Bong\\_Wi\\_Final\\_Report.pdf](http://www.nasa.gov/sites/default/files/files/Bong_Wi_Final_Report.pdf)).
- [10] J. Herring, et al., Staring 256 × 256 LWIR focal plane array performance of the Raytheon exoatmospheric kill vehicle, in: Conference Proceedings, 1998, Print.
- [11] A.M. Sessler, et al., Countermeasures: a technical evaluation of the operational effectiveness of the planned US national missile defense system, Union of Concerned Scientists MIT Security Studies Program, Cambridge, April 2000.
- [12] D. Wilkening, Making sense of ballistic missile defense: an assessment of concepts and systems for U.S. boost-phase missile defense in comparison to other alternatives, in: American Physical Society Nuclear Workshop, George Washington University, 1–2 November 2013.
- [13] J. Lyzhoft, D. Groath, B. Wie, Optical and infrared sensor fusion for hypervelocity asteroid intercept guidance, AAS 14-421, AAS/AIAA Space Flight Mechanics Meeting, Santa Fe, NM, 26–30 January 2014.
- [14] WISE Preliminary Release Explanatory Supplement: WISE Flight System and Operations, WISE Preliminary Release Explanatory Supplement, N.p., 12 April 2011, Web, 7 April 2014, ([http://wise2.ipac.caltech.edu/docs/release/prelim/expsup/sec3\\_2.html](http://wise2.ipac.caltech.edu/docs/release/prelim/expsup/sec3_2.html)).
- [15] J.D. Beish, Cassegrain telescopes for amateurs, 26 September, 2014, ([http://www.alpo-astronomy.org/jbeish/Cass\\_Equ.pdf](http://www.alpo-astronomy.org/jbeish/Cass_Equ.pdf)).
- [16] J.A. Shaw, Reflector Telescopes, Class Lecture, Optical System Design, Montana State University, Bozeman, 4 February 2009.
- [17] M.E. Lockwood, Cassegrain Formulas and Tips by Mike Lockwood, Lockwood Custom Optics, N.p., n.d. Web, 5 May 2014, (<http://www.loptics.com/ATM/mirrormaking/cassinfo/cassinfo.html>).
- [18] Richard S. Quimby, Photonics and Lasers: An Introduction, Wiley-Interscience, Hoboken, NJ, 2006.
- [19] L.A. Lebofsky, J.R. Spencer, Radiometry and thermal modeling of asteroids, in: R.P. Binzel, T. Gehrels, M.S. Matthews (Eds.), In Asteroids II, University of Arizona Press, Tucson, 1989, pp. 128–147.
- [20] J.H. Rieke, Detection of Light: From the Ultraviolet to the Submillimeter, 1st ed. Cambridge University Press, New York, 1994, 56.
- [21] Justin C. Dunlap, et al., Dark current behavior in DSLR cameras, in: IS&T/SPIE Electronic Imaging, International Society for Optics and Photonics, 2009.
- [22] William C. Porter, et al., Dark current measurements in a CMOS imager, in: Electronic Imaging 2008, International Society for Optics and Photonics, 2008.
- [23] Michael E. Ressler, et al., Performance of the JWST/MIRI Si:As detectors, in: SPIE Astronomical Telescopes + Instrumentation, International Society for Optics and Photonics, 2008.
- [24] Steve B. Howell, Handbook of CCD Astronomy, vol. 5, Cambridge University Press, Cambridge, UK, New York, 2006.
- [25] F.J. Morin, J.P. Maita., Electrical properties of silicon containing arsenic and boron, *Phys. Rev.* 96.1 (1954) 28.
- [26] Helmut Budzier, Gerald Gerlach, Thermal Infrared Sensors: Theory, Optimisation and Practice, Wiley, Chichester, West Sussex, UK, Hoboken, N.J.
- [27] M. Bolte, Signal-to-noise in optical astronomy, Class Lecture, Modern Observational Techniques, University of California, Santa Cruz, 2004.
- [28] E.L. Dereniak, G.D. Boreman, *Infrared Detectors and Systems*, John Wiley & Sons, New York, 1996 (Chapter 5).
- [29] B. Kaplinger, Physical modeling and high-performance GPU computing for characterization interception, and disruption of hazardous near-Earth objects (Ph.D. thesis), Iowa State University, 2013.
- [30] A.J. Fenn, Near-field testing of adaptive radar systems, *Linc. Lab. J.* 3 (1) (1990) 23–40.
- [31] Amanda K. Mainzer, et al., Preliminary design of the wide-field infrared survey explorer (WISE), in: Optics & Photonics 2005, International Society for Optics and Photonics, 2005.
- [32] III. WISE Flight System and Operations (WISE All-Sky Release Explanatory Supplement: Flight System and Operations), ([http://wise2.ipac.caltech.edu/docs/release/allsky/expsup/sec3\\_2.html](http://wise2.ipac.caltech.edu/docs/release/allsky/expsup/sec3_2.html)).
- [33] Edward L. Wright, et al., The Wide-field Infrared Survey Explorer (WISE): mission description and initial on-orbit performance, *Astron. J.* 140 (6) (2010), 1868.
- [34] Elisabetta Dotto, Observations of asteroids in the thermal infrared, in: Regolith on Solar System Bodies, INAF – Observatory of Rome (Italy), Observatoire de Paris CIAS, 1–3 December 2010.
- [35] Daniela Lazzaro, Julio Angel Fernández, Asteroids, Comets, and Meteors (IAU S229), No. 229, Cambridge University Press, Cambridge, UK, New York, NY, 2006.
- [36] Lucy F. Lim, et al., Thermal infrared (813 m) spectra of 29 asteroids: the Cornell mid-infrared asteroid spectroscopy (MIDAS) survey, *Icarus* 173 (2) (2005), 385–408.
- [37] A. Maturilli, et al., A spectral library of emissivity measurements for asteroid analogs, in: Lunar and Planetary Science Conference, vol. 45, 2014.
- [38] B. Zimmerman, B. Wle, GPU-Accelerated computational tool development for studying the effectiveness of nuclear subsurface explosions, IAA-PDC, Frascati Italy, 2015, 13–17.